Journal of Rock Mechanics and Geotechnical Engineering 16 (2024) 1280–1288

Contents lists available at ScienceDirect

Journal of Rock Mechanics and Geotechnical Engineering

journal homepage: www.jrmge.cn

Full Length Article

Spalling characteristics of high-temperature treated granitic rock at different strain rates

L.F. Fan*, Q.H. Yang, X.L. Du

The Key Laboratory of Urban Security and Disaster Engineering of Ministry of Education, Beijing University of Technology, Beijing, 100124, China

ARTICLE INFO

Article history:
Received 1 February 2023
Received in revised form
23 April 2023
Accepted 15 May 2023
Available online 4 September 2023

Keywords:
Dynamic spalling characteristics
High temperature
Strain rate
Dynamic loading
Granite

ABSTRACT

The dynamic spalling characteristics of rock are important for stability analysis in rock engineering. This paper presented an experimental investigation on the dynamic spalling characteristics of granite with different temperatures and strain rates. A series of dynamic spalling tests with different impact velocities were conducted on thermally treated granite at different temperatures. The dynamic spalling strengths of granite with different temperatures and strain rates were determined. A model was proposed to correlate the dynamic spalling strength of granite, high temperature and strain rate. The results show that the spalling strength of granite decreases with increasing temperature. Moreover, the spalling strength of granite with a higher strain rate is larger than that with a lower strain rate. The proposed model can describe the relationship among dynamic spalling strength of granite, high temperature and strain rate.

1. Introduction

Tensile stress is generated by the reflection of a stress wave on the joint and free surfaces of a rock mass (Li and Ma, 2009; Chen et al., 2015; Li et al., 2017; Xie et al., 2020; Huang et al., 2022). The spalling failure of the rock mass induced by tensile stress cannot be ignored because the tensile strength of the rock mass is much lower than the compressive strength of the rock mass (Cai, 2010). In addition, the rock mass is generally influenced by the high temperature in temperature-related rock engineering, such as geothermal energy development and the underground disposal of nuclear waste. High temperatures can influence the material characteristics of a rock mass (Rang and Sun, 2012; Liu and Xu, 2013; Fan et al., 2017; Yin et al., 2021; Li et al., 2022). Therefore, it is important to investigate the dynamic spalling characteristics of rock masses at high temperatures for the safety of rock engineering.

The spalling method was generally utilized to investigate the dynamic spalling characteristics of brittle materials (Khosravani et al., 2019; Erzar and Forquin, 2011; Huang et al., 2021a). The tensile stress was generated by the superposition of a compression wave and tensile wave in this spalling method. A spalling fracture of the brittle material occurred when the maximum tensile stress exceeded the spalling strength (Erzar and Forquin, 2010; Zhu et al., 2011). The advantage of the spalling method was that the brittle material was always subjected to uniaxial tensile stress when spalling occurred. The spalling method has been adopted to investigate the spalling strength of brittle materials such as concrete (Klepaczko and Brara, 2001; Zhang et al., 2020; Wang et al., 2021). Their research showed that the spalling strength of the concrete was significantly affected by the strain rate. The spalling method was adopted to reveal the spalling strength of brittle materials with different strain rates (Wu et al., 2005, 2018; Wang and Yang, 2015). Their research showed that the spalling strength under a higher strain rate was higher than that under a lower strain rate for brittle materials. The spalling method was further developed by combining it with a high-speed photography system to investigate the spalling behavior of brittle materials (Klepaczko and Brara, 2001; Khosravani et al., 2019; Forquin et al., 2019; Lukic et al., 2020). Previous research showed that the spalling method could reliably obtain the dynamic spalling characteristics of brittle materials.

The spalling characteristics of rock masses have been extensively investigated (Mitelman and Elmo, 2016; Li et al., 2017, 2018; Niu et al., 2018; Tao et al., 2019). A spalling test was applied to study the spalling strength of a rock mass (Khan and Iran, 1987; Saadati et al., 2016; Forquin et al., 2022). This research showed that the dynamic spalling strength of the rock mass was higher than the

* Corresponding author.
E-mail address: fanlifeng@bjut.edu.cn (L.F. Fan).

Peer review under responsibility of Institute of Rock and Soil Mechanics, Chinese Academy of Sciences.

https://doi.org/10.1016/j.jrmge.2023.05.016

quasi-static spalling strength of the rock mass. The relationship between the spalling strength of the rock mass and its strain rate was investigated based on spalling tests with different impact velocities (Cho et al., 2003; Huang et al., 2021b). This research showed that a larger spalling strength was achieved under a higher strain rate for the rock mass. The spalling strength of the rock mass with different pre-confining pressures was experimentally investigated (Zhao et al., 2019). This research showed that the spalling strength initially increased and then decreased with increasing pre-confining pressure for the rock mass. Previous investigations focused on the dynamic spalling characteristic of the rock mass at room temperature. The rock mass was generally influenced by the high temperature (Liu and Xu, 2015; Fan et al., 2018; Pathiranagei and Gratchev, 2022). High temperature induced the generation of microdefects in rock masses which affected the dynamic mechanical properties of rock masses (Meyers 1994; Abdollahipour et al., 2016;Abdollahipour and Marji, 2020; Lak et al., 2019; Wu et al., 2022; Zhang et al., 2021). Therefore, the effect of high temperature on the spalling characteristics of rock masses needs to be further explored.

In the present study, spalling tests with different impact velocities were performed to study the spalling characteristics of granite under heat treatment. The spalling strength of granite was determined. The relationships among spalling strength, high temperature and strain rate were revealed. A model was developed to correlate the spalling strength of granite, temperature and strain rate.

2. Procedure of spalling test

Spalling failure was generated by the superposition of the incident compression wave and reflected tensile wave, as shown in Fig. 1. The spalling test was performed to study the spalling characteristics of the rock mass at different temperatures.

2.1. Specimen preparation

The cylindrical specimens adopted for the dynamic spalling test were obtained from Fujian, China. The density of granite was 2665.3 kg/m^3 and the porosity of granite was 0.87%. The granite was mainly composed of quartz, feldspar and biotite. The diameter of the specimen was designed as 4.5 cm, which was much smaller than the wavelength (at least 139 cm) to satisfy the one-dimensional wave propagation theory. The length of the specimen was designed as 120 cm, which ensured that the tensile stress was generated by the wave superposition. The two free surfaces of the granite bar were carefully ground to ensure coupling with the incident bar and assure the complete reflection of the stress wave. Macro-cracks in the rock mass could affect the experimental results, thus all granite bars were carefully checked to ensure that there were no obvious macro-cracks. To avoid the contingency of the experimental phenomenon caused by specimens, three specimens were prepared under the same experimental conditions.

2.2. Thermal treatment

High temperature can influence the dynamic mechanical properties of a rock mass, as shown in Fig. 2. Five temperatures of 25 °C, 100 °C, 200 °C, 300 °C and 400 °C were adopted in the present study. Granite bars were uniformly heated to the set temperature by the thermal treatment setup. According to previous research, the heating rate was set to 2 °C/min to avoid the effect of thermal shock on the mechanical properties of granite (Shao et al., 2015; Yang et al., 2017; Rossi et al., 2018). Then, granite bars were heated at the designed temperature for 4 h to ensure the same temperature inside the granite bars. Finally, the granite bars were naturally cooled from the set temperature to room temperature.

2.3. The dynamic spalling test

The dynamic spalling test utilized the superposition of the compression wave and tensile wave to generate the tensile stress. Spalling failure occurred when the maximum tensile stress exceeded the spalling strength of the material. Fig. 3 shows the dynamic spalling system. The dynamic spalling system included the impact subsystem and data collection system. In the impact subsystem, an incident bar with a length of 2.5 m was applied for stress wave propagation. A fusiform striker was applied to generate the stress wave. The impact velocity of the fusiform striker is related to the air pressure of the gas gun. The impact velocity increases as the air pressure of the gas gun increases. The impact velocity can be determined by the speed sensor. The impact velocities generated by air pressure of 0.3 MPa, 0.35 MPa and 0.4 MPa were 5.52 m/s, 6.02 m/s and 6.53 m/s, respectively.

In the data collection subsystem, a LK2107 dynamic strain instrument and strain gauge were adopted to obtain the incident, reflected and transmitted stress waves. The sampling rate of the dynamic strain instrument increased as the sampling time decreased. The higher sampling rate resulted in a shorter sampling time. The lower sampling rate caused the collected stress waves to have lower accuracy. Stress waves were obtained at a sampling rate of 1×10^7 and a sampling time of 12 ms. Three groups of strain gauges were used to obtain stress waves. A group of strain gauges installed on the incident bar was used to obtain the incident stress wave and reflected stress wave. In addition, a strain gauge was adopted to generate trigger signals for the dynamic strain instrument. The other two groups of strain gauges were installed on the granite bar to obtain the propagation of the transmitted stress

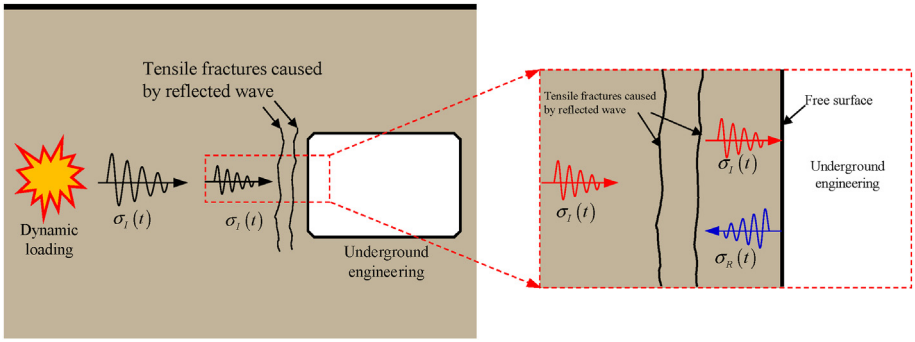

Fig. 1. Schematic diagram of tensile fracture generation caused by the stress wave.

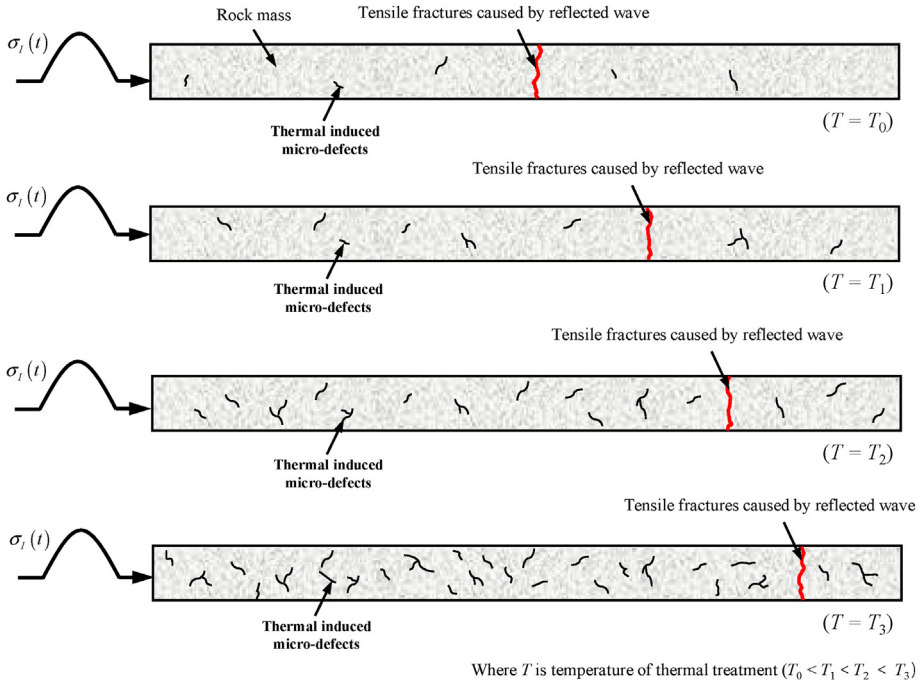

Fig. 2. Schematic diagram of dynamic tensile failure of rock mass with different temperatures.

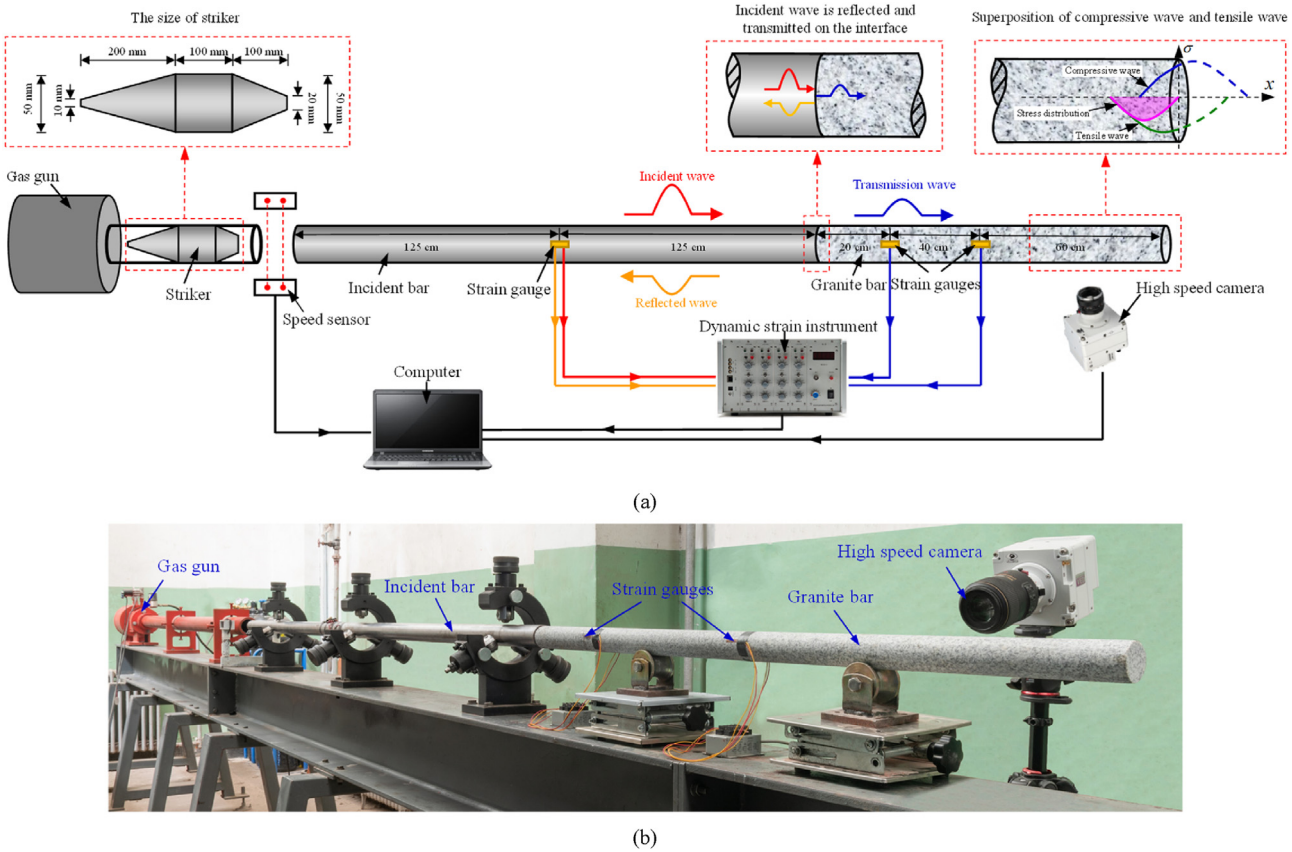

Fig. 3. The dynamic loading system combined with high-speed digital image correlation (H-DIC) for the dynamic spalling test: (a) Schematic diagram of dynamic spalling tests, and (b) Experimental setup for the dynamic spalling test.

wave. To separate the compressive wave and tensile wave, the strain gauge should be positioned close to the incident end (Rang and Sun, 2012; Wu et al., 2018). Strain gauges were positioned at distances of 20 cm and 60 cm from the incident end.

In the data collection subsystem, a high-speed camera was used to determine the location of the first spalling. The high-speed camera was a Phantom VEO 710 L. The frame rate of the high-speed camera decreased as the resolution increased. The location of the first spalling cannot be determined for the lower frame rate. To improve the accuracy of displacement determined by the image and distinguish the first spalling from other spalling, a high-speed camera with a resolution of 1024 × 80 pixels and a frame rate of 86,000 frames per second was used to collect the process of spalling. The shooting area was the half of the granite bar near the free end where the first spalling occurred. Digital image correlation (DIC) was used to determine the displacement field of a specimen by comparing the digital images taken before and during the dynamic spalling test (Zhao and Zhao, 2012; Chi et al., 2019; Li et al., 2022). DIC analysis was applied to the obtained images to determine the location of the first spalling based on the displacement field of the granite bar. A spatial resolution of 0.56 mm/pixel, a subset size of 21 × 21 pixels and a step size of 4 pixels were used to carry out DIC analysis.

Fig. 3 also shows the procedure of the spalling test for granite bars with different heat treatments. The position of the incident bar was adjusted before the spalling test to ensure that the incident bar, striker and specimen were aligned. The incident bar was well coupled with the specimen to avoid the concentration of stress. The fusiform striker was pushed by gas gun and impacted the incident bar. The incident stress wave was generated by the collision between the fusiform striker and the incident bar. At the interface between the incident bar and the granite bar, the incident stress wave was reflected and transmitted due to the difference between the wave impedance of the incident bar and the granite bar. The transmitted compression wave propagated into the granite bar. The transmitted compression wave was reflected as the tensile wave at the free end of the granite bar. The tensile stress was produced by the superposition of the compression wave and tensile wave. The spalling failure occurred when the maximum tensile stress exceeded the spalling strength of the high-temperature granite. The high-speed camera was applied to obtain the process of spalling. The DIC algorithm was performed on the obtained images to determine the location of the first spalling.

3. Determination of dynamic spalling strength for high-temperature granite

An attenuation of the stress wave occurs in the high-temperature granite, which causes difference between the stress wave at the location of the strain gauges and the stress wave at the location of the first spalling. The propagation coefficient (attenuation coefficient and wave number) is applied to predict the propagation of the stress wave (Li et al., 2015, 2019; Niu et al., 2020; Fan et al., 2021). Based on wave propagation theory, the strain and stress in a high-temperature granite bar can be determined as

$$\varepsilon_1(x,t) = F^{-1}[\tilde{\varepsilon}_\mathrm{I}(w)\mathrm{e}^{-\gamma x}] \tag{1}$$

$$\sigma_1(x,t) = F^{-1}\left[-\frac{\rho\omega^2}{\gamma^2}\tilde{\varepsilon}_\mathrm{I}(w)\mathrm{e}^{-\gamma x}\right] \tag{2}$$

where ε_1 and σ_1 are the strain and stress generated by the incident stress wave in the high-temperature granite bar, respectively; x is the location of the cross-section for the high-temperature granite bar; t is the time of stress wave propagation; $\tilde{\varepsilon}_\mathrm{I}$ is the measured strain pulse applied Fourier transformation; ρ is the density of the high-temperature granite; ω is the angular frequency; γ is the propagation coefficient; and F^{-1} is the application of the inverse Fourier transform.

The propagation coefficient can be expressed as

$$\gamma(\omega) = \alpha(\omega) + \mathrm{i}k(\omega) \tag{3}$$

where α and k are the attenuation coefficient and the wave number of the stress wave in high-temperature granite, respectively.

The attenuation coefficient and wave number can be expressed as

$$\alpha = -\mathrm{Re}\left[\ln\frac{1}{l}\left(\frac{F|\varepsilon_\mathrm{n}|}{F|\varepsilon_\mathrm{p}|}\right)\right] \tag{4}$$

$$k = -\mathrm{Im}\left[\ln\frac{1}{l}\left(\frac{F|\varepsilon_\mathrm{n}|}{F|\varepsilon_\mathrm{p}|}\right)\right] \tag{5}$$

where ε_p is the positive wave produced by the direct impact of the pendulum hammer, ε_n is the negative wave produced by the reflection of the positive wave at the free end, l is the wave propagation distance, and F is the application of the Fourier transform (Butt et al., 2015; Li et al., 2019; Wang et al., 2022a).

The incident stress wave propagates to the free end of the high-temperature granite bar and is reflected as the reflected stress wave. The strain and stress generated by the reflected stress wave in the high-temperature granite bar can be expressed as

$$\varepsilon_2(t) = F^{-1}\left[-\tilde{\varepsilon}_\mathrm{I}(w)\mathrm{e}^{-\gamma(2L-x)}\right] \tag{6}$$

$$\sigma_2(t) = F^{-1}\left[\frac{\rho\omega^2}{\gamma^2}\tilde{\varepsilon}_\mathrm{I}(w)\mathrm{e}^{-\gamma(2L-x)}\right] \tag{7}$$

where ε_2 and σ_2 are the strain and stress generated by the reflected stress wave in the high-temperature granite bar, respectively; and L is the distance from the strain gauge to the free end.

The strain and stress in the high-temperature granite bar under the superposition of the incident stress wave and the reflected stress wave can be expressed as

$$\varepsilon_3(x,t) = \varepsilon_1(x,t) + \varepsilon_2(x,t) \tag{8}$$

$$\sigma_3(x,t) = \sigma_1(x,t) + \sigma_2(x,t) \tag{9}$$

where ε_3 and σ_3 are the strain and stress generated by the superposition of the incident stress wave and the reflected stress wave in the high-temperature granite bar, respectively.

The stress distribution can be determined based on Eq. (9). The spalling strength is determined based on the stress distribution and the location of the first spalling.

The strain rate of the spalling process can be expressed as

$$\dot{\varepsilon} = \frac{\varepsilon_\mathrm{s}}{\tau} \tag{10}$$

where $\dot{\varepsilon}$ is the strain rate, ε_s is the strain of spalling failure, and τ is the time between the tensile stress occurrence and spalling failure.

4. Results and discussion

4.1. The transmission wave in high-temperature granite bar

Fig. 4 shows the transmitted stress wave generated by the striker with different impact velocities in the high-temperature granite bar. In Fig. 4a–c, the impact velocities are 5.52 m/s,

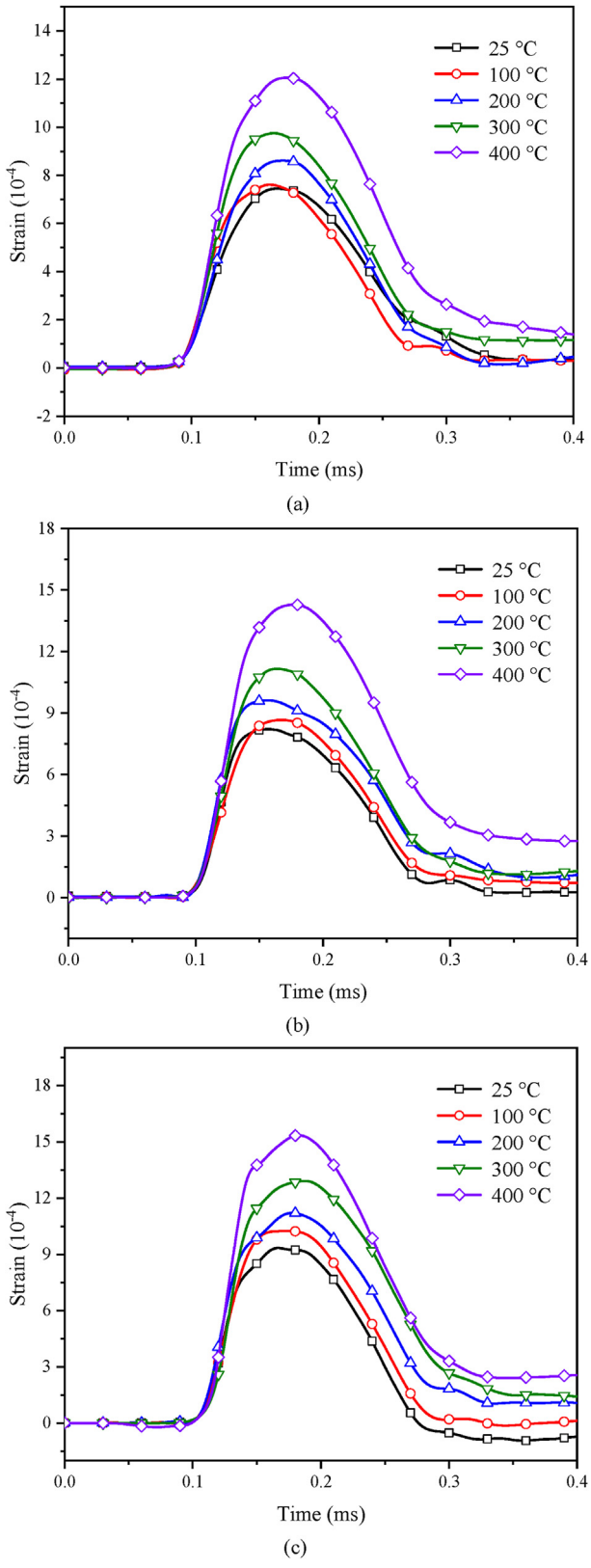

Fig. 4. Stress wave generated by different impact velocities in thermally treated granite: (a) 5.52 m/s, (b) 6.02 m/s, and (c) 6.53 m/s.

6.02 m/s and 6.53 m/s, respectively. The amplitude of the transmitted stress wave increases with increasing temperature, as shown in Fig. 4. For example, the amplitude of the transmitted stress wave increases from 7.45 × 10^{-4} to 12.05 × 10^{-4} as the temperature increases from 25 °C to 400 °C under an impact velocity of 5.52 m/s, as shown in Fig. 4a. This is mainly because the wave velocity of granite decreases as the temperature increases, resulting in a decrease in the wave impedance of granite. The wave impedance ratio of the incident bar and granite bar increases as the temperature increases. The amplitude of the transmitted wave increases as the wave impedance ratio increases (Wang et al., 2022b). Therefore, the amplitude of the transmitted wave with a higher temperature is larger than that with a lower temperature. The amplitude of the transmitted stress wave under a higher impact velocity is larger than that under a lower impact velocity for a fixed temperature. For the granite bar with a heat treatment of 200 °C, the amplitude of the transmitted stress wave obtained by the striker with an impact velocity of 6.53 m/s is 11.21 × 10^{-4} which is 30.2% larger than that of the transmitted stress wave obtained by the striker with an impact velocity of 5.52 m/s.

4.2. Propagation coefficient of the high-temperature granite

The stress wave obtained by strain gauges is different from that at the location of the first spalling because of the wave attenuation in granite with heat treatment. The propagation coefficient (attenuation coefficient and wave number) is applied to predict the stress wave propagation. Fig. 5 shows the variation in the propagation coefficient with increasing frequency in high-temperature granite.

Fig. 5a shows the variation in the attenuation coefficient with increasing frequency in granite under different heat treatments. The attenuation coefficient increases with increasing frequency, which indicates that the attenuation of the harmonic wave with a higher frequency is faster than that of the harmonic wave with a lower frequency. It is also observed that a higher temperature results in a larger attenuation coefficient. The attenuation of the harmonic wave is faster in granite with higher temperature. The wave attenuation caused by the high temperature should be considered for the determination of the spalling strength.

Fig. 5b shows the variation in wave number with increasing frequency in granite with different heat treatments. The wave number increases with increasing frequency. It is also observed that a higher temperature results in a larger wave number.

4.3. The first spalling of the high-temperature granite bar

Fig. 6 shows the typical variation in the displacement of the heated granite bar as time increases. Fig. 6a shows the variation in the displacement fields of the heated granite bar as time increases. The displacement fields of the high-temperature granite bar increase with increasing time. The displacement near the free end is larger than that far from the free end.

Fig. 6b shows the relationship between the displacement generated by the impact and the distance to the free end. The displacement generated by the impact decreases as the distance to the free end increases. When the time is 0.2552 ms, the displacement for the distance of 10 cm to the free end is 0.603 mm, which increases by 21.8% compared with 0.495 mm for the distance of 30 cm to the free end. It is also observed that the displacement increases slowly as the distance to the free end decreases. Then, the

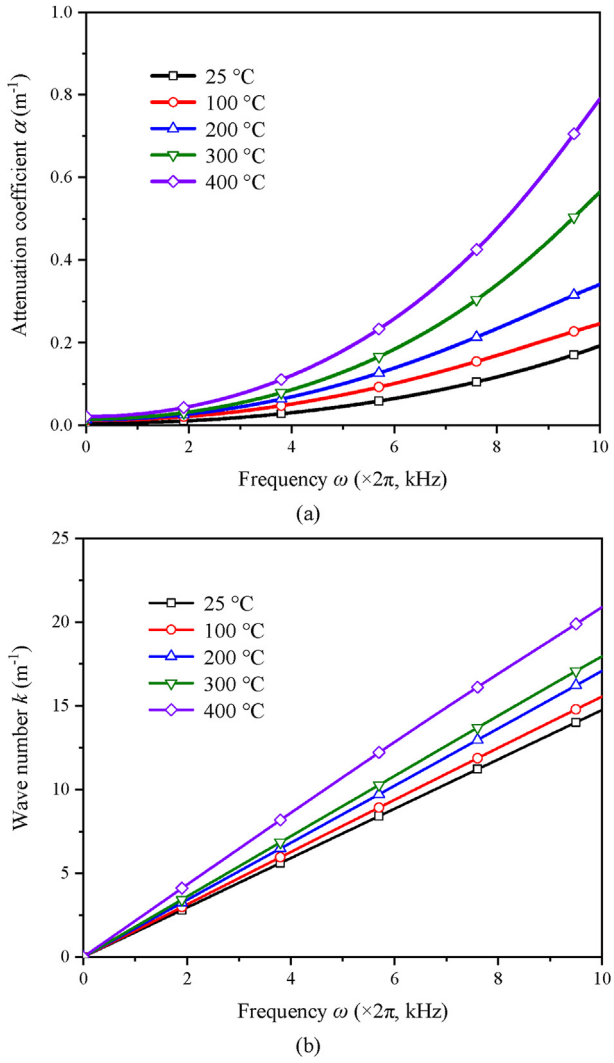

Fig. 5. Propagation coefficient of stress wave in high-temperature granite for prediction of the stress wave: (a) Attenuation coefficient, and (b) Wave number.

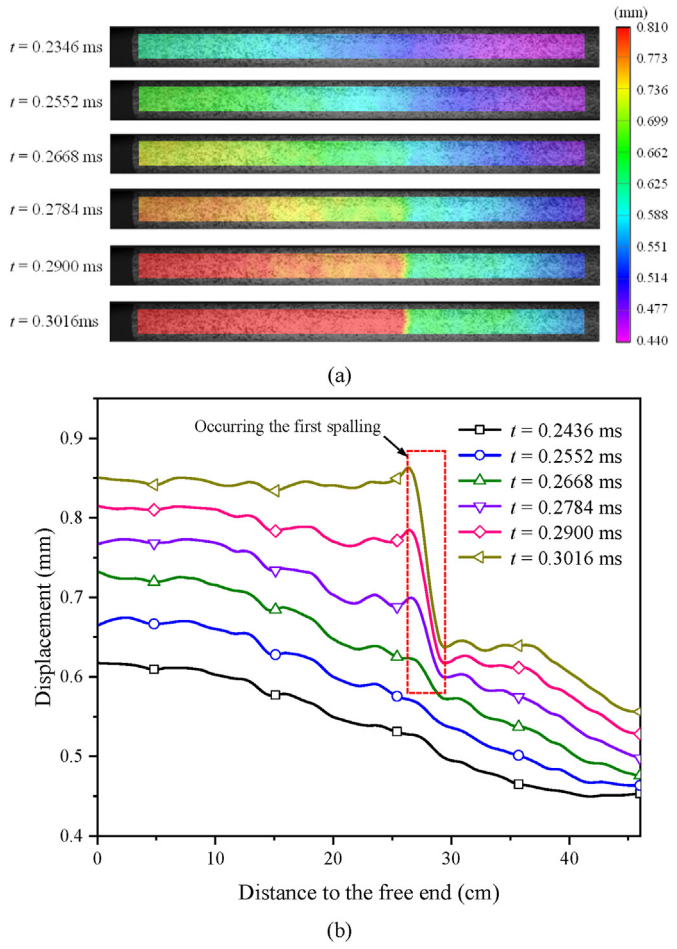

Fig. 6. Determination of the location of the first spalling: (a) Variation in the displacement field for granite, and (b) Displacement evolution of granite experiencing the first spalling.

displacement increases sharply for a distance of 28.1 cm to the free end. The displacement of the granite bar generated by impact comes from continuous variation to discontinuous variation. This result further indicates that the first spalling occurs at this location.

Fig. 7 shows the location of the first spalling for the thermally treated granite bar. The spalling fracture is relatively flat and there is no obvious scratch. The results indicate that the spalling fracture is not subject to shear stress. The spalling fracture is approximately perpendicular to the axis of the granite bar. The results indicate that the tensile stress is parallel to the axis of the granite bar. It is also observed that the location of the first spalling is at a distance of 23.5–32.7 cm away from the free end, which is in the superposition range of the compression wave and tensile wave.

4.4. Dynamic spalling strength of high-temperature granite with different strain rates

Fig. 8 shows the typical relationship between the stress distribution of the granite bar and time. The compression wave first propagates through the granite bar. The granite bar is mainly subjected to compression stress. The incident compression wave arrives at the free end of the granite bar and is reflected as the tensile wave as time increases. Then, the reflected tensile wave propagates to the incident end of the granite bar. Tensile stress is generated by wave superposition. The range subjected to tensile stress increases with increasing time. The maximum compressive stress of the granite bar decreases as time increases, while the maximum tensile stress of the granite bar increases as time increases. The distance between the location of the maximum tensile stress and the free end increases as time increases. The first spalling failure of the granite bar occurs when the maximum tensile stress exceeds the spalling strength.

Fig. 9 shows the relationship between the spalling strength of high-temperature granite and strain rate. The spalling strength of the granite with heat treatment increases with increasing strain rate, as shown in Fig. 9. For the high-temperature granite at 100 °C, the spalling strength of the granite under a strain rate of 12 s^{-1} is 24.6 MPa, which increases 42.7% to 35.1 MPa under a strain rate of 25.1 s^{-1}. In addition, the spalling strength is obviously temperature dependent. The higher temperature results in the smaller spalling strength of the granite. For example, for a strain rate of 11.5 s^{-1}, the spalling strength of the granite is 22.1 MPa under a heat treatment of 200 °C, it decreases by 19% to 17.9 MPa under a heat treatment of 400 °C.

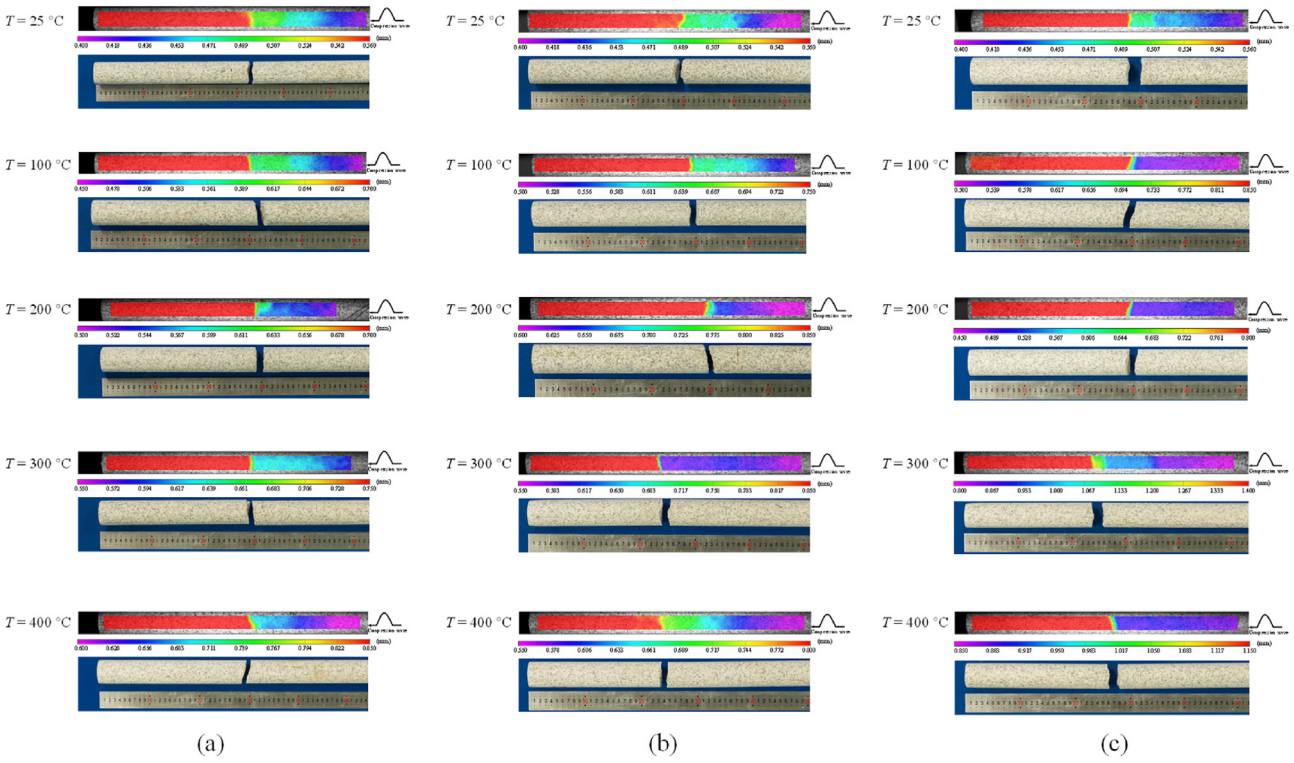

Fig. 7. Location of the first spalling for granite with high-temperature treatment under different impact velocities: (a) 5.52 m/s, (b) 6.02 m/s, and (c) 6.53 m/s.

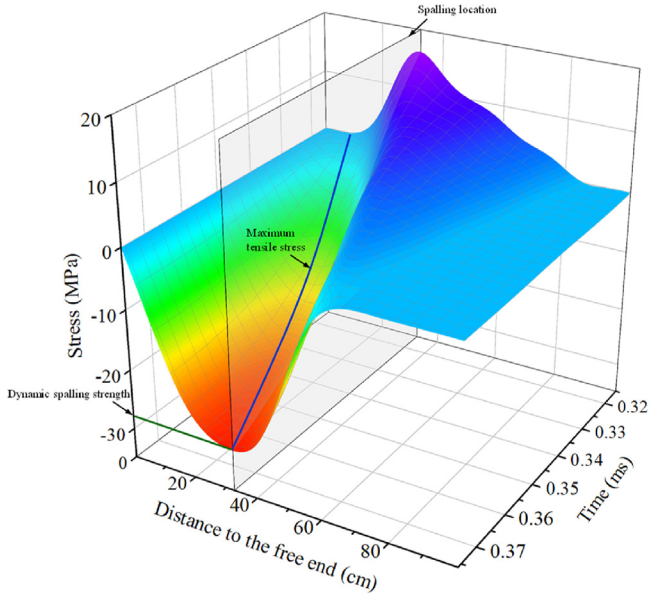

Fig. 8. Determination of dynamic spalling strength for granite with high-temperature treatment.

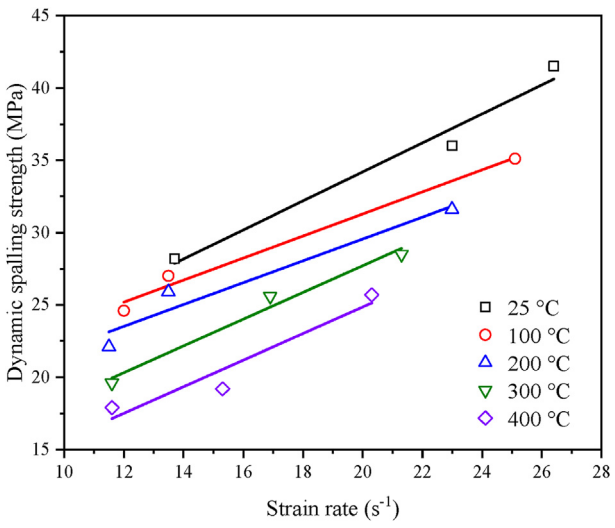

Fig. 9. Relationship between the dynamic spalling strength of the high-temperature granite and strain rate.

4.5. The model of dynamic spalling strength under high temperature and strain rate effects

The experimental results show that the dynamic spalling strength is related to the temperature and strain rate. A model describing the relationships among the dynamic spalling strength, the temperature and strain rate was proposed. The model is expressed as

$$\sigma_{\text{spall}}(T,\dot{\varepsilon}) = a_T T^{p_1} + a_{\dot{\varepsilon}}\dot{\varepsilon}^{p_2} + a_{T\dot{\varepsilon}} T^{p_3}\dot{\varepsilon}^{p_4} \tag{11}$$

where σ_{spall} is the spalling strength of the high-temperature granite; $\dot{\varepsilon}$ is the strain rate; T is the temperature; and a_T, $a_{\dot{\varepsilon}}$, $a_{\dot{\varepsilon}T}$, p_1, p_2, p_3 and p_4 are the material parameters of the high-temperature granite. The material parameters of the high-temperature granite determined by the least square method are listed in Table 1. The mode considers the three effects, including the effect of temperature, the effect of strain rate, and the combined effects of temperature and strain rate.

Table 1
Material parameters of the function relationship determined by the spalling tests.

a_T	$a_{\dot{\varepsilon}}$	$a_{T\dot{\varepsilon}}$	p_1	p_2	p_3	p_4
-1.26×10^4	8.06×10^6	-2.94×10^3	1.01	4.91×10^{-1}	1.03	4.85×10^{-1}

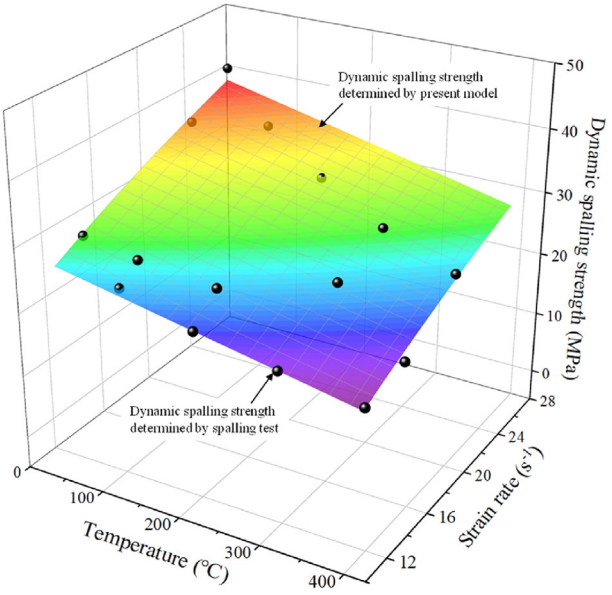

Fig. 10. Comparison between the dynamic spalling strength determined by the present model and that determined by the spalling test.

Fig. 10 shows the comparison between the spalling strength determined by the present model and that determined by the spalling test. The spalling strength decreases with increasing temperature when the strain rate is constant. The spalling strength increases with increasing strain rate when the temperature is constant. The dynamic spalling strength rapidly increases under combined effects of lower temperature and higher strain rate. In addition, the spalling strength obtained by the present model is similar to the spalling strength obtained by the spalling test, with an accuracy of $R^2 = 0.975$.

5. Conclusions

The dynamic spalling characteristics of granite with different temperatures and strain rates were investigated. Spalling tests with different impact velocities were performed on high-temperature granite. The influence of the high temperature on the dynamic spalling strength of granite was investigated. A model was proposed to correlate dynamic spalling strength of granite, high temperature and strain rate. The main conclusions are drawn as follows:

(1) The amplitude of the transmission stress wave is related to temperature. The amplitude of the transmission stress wave increases with increasing temperature.
(2) Based on the stress distribution determined by propagation coefficient and first spalling location determined by high-speed camera system, the dynamic spalling strength of granite with different temperatures and strain rates can be obtained.
(3) The dynamic spalling strength of the granite is significantly influenced by the temperature. The dynamic spalling strength of the granite decreases with increasing temperature.
(4) The dynamic spalling strength of the granite is sensitive to strain rate. The dynamic spalling strength of the granite increases with increasing strain rate.
(5) The proposed model can correlate the dynamic spalling strength of granite, temperature and strain rate. The spalling strength determined by the proposed model is similar to that determined by the spalling test, with an accuracy of $R^2 = 0.975$.

Declaration of competing interest

The authors declare that they have no known competing financial interests or personal relationships that could have appeared to influence the work reported in this paper.

Acknowledgments

This work is supported by the Beijing Natural Science Foundation, China (Grant No. JQ20039) and National Natural Science Foundation of China (Grant No. 12172019).

References

Abdollahipour, A., Marji, M.F., Bafghi, A.Y., Gholamnejad, J., 2016. Time-dependent crack propagation in a poroelastic medium using a fully coupled hydromechanical displacement discontinuity method. Int. J. Fract. 199 (1), 71–87.
Abdollahipour, A., Marji, M.F., 2020. A thermo-hydromechanical displacement discontinuity method to model fractures in high-pressure, high-temperature environments. Renew. Energy 153, 1488–1503.
Butt, H.S.U., Xue, P., Jiang, T.Z., Wang, B., 2015. Parametric identification for material of viscoelastic SHPB from wave propagation data incorporating geometrical effects. Int. J. Mech. Sci. 91, 46–54.
Cai, M., 2010. Practical estimates of tensile strength and Hoek-Brown strength parameter $m(i)$ of brittle rocks. Rock Mech. Rock Eng. 43 (2), 167–184.
Chen, X., Li, J.C., Cai, M.F., Zou, Y., Zhao, J., 2015. Experimental study on wave propagation across a rock joint with rough surface. Rock Mech. Rock Eng. 48 (6), 2225–2234.
Chi, L.Y., Zhang, Z.X., Aalberg, A., Yang, J., Li, C.C., 2019. Fracture processes in granite blocks under blast loading. Rock Mech. Rock Eng. 52 (3), 853–868.
Cho, S.H., Ogata, Y., Kaneko, K., 2003. Strain-rate dependency of the dynamic tensile strength of rock. Int. J. Rock Mech. Min. Sci. 40 (5), 763–777.
Erzar, B., Forquin, P., 2010. An experimental method to determine the tensile strength of concrete at high rates of strain. Exp. Mech. 50 (7), 941–955.
Erzar, B., Forquin, P., 2011. Experiments and mesoscopic modelling of dynamic testing of concrete. Mech. Mater. 43 (9), 505–527.
Fan, L.F., Wu, Z.J., Wan, Z., Gao, J.W., 2017. Experimental investigation of thermal effects on dynamic behavior of granite. Appl. Therm. Eng. 125, 94–103.
Fan, L.F., Gao, J.W., Wu, Z.J., Yang, S.Q., Ma, G.W., 2018. An investigation of thermal effects on micro-properties of granite by X-ray CT technique. Appl. Therm. Eng. 140, 505–519.
Fan, L.F., Yang, K.C., Wang, M., Wang, L.J., Wu, Z.J., 2021. Experimental study on wave propagation through granite after high-temperature treatment. Int. J. Rock Mech. Min. Sci. 148, 104946.
Forquin, P., Lukic, B., Saletti, D., Sallier, L., Pierron, F., 2019. A benchmark testing technique to characterize the stress-strain relationship in materials based on the spalling test and a photomechanical method. Meas. Sci. Technol. 30 (12), 125006.
Forquin, P., Saadati, M., Saletti, D., Lukic, B., Schiaffini, F., Weddfelt, K., Larsson, P.L., 2022. Investigation of the mechanical behaviour of lingulid sandstone emphasizing the influence from pre-existing structural defects-part 2: dynamic testing and numerical modelling. Appl. Sci.-Basel 12 (22), 11621.
Huang, X.P., Kong, X.Z., Chen, Z.Y., Fang, Q., 2021a. Peridynamics modelling of dynamic tensile failure in concrete. Int. J. Impact Eng. 155, 103918.
Huang, J., Liu, X.L., Song, D.Q., Zhao, J., Wang, E.Z., Zhang, J.M., 2022. Laboratory-scale investigation of response characteristics of liquid-filled rock joints with different joint inclination under dynamic loading. J. Rock Mech. Geotech. Eng. 14 (2), 396–406.
Huang, L.Q., Wang, J., Momeni, A., Wang, S.F., 2021a. Spalling fracture mechanism of granite subjected to dynamic tensile loading. Trans. Nonferrous Metals Soc. China 31 (7), 2116–2127.
Khan, A.S., Iran, F.K., 1987. An experimental-study of stress wave transmission at a metallic-rock interface and dynamic tensile failure of sandstone, limestone, and granite. Mech. Mater. 6 (4), 285–292.
Klepaczko, J.R., Brara, A., 2001. An experimental method for dynamic tensile testing of concrete by spalling. Int. J. Impact Eng. 25 (4), 387–409.

Khosravani, M.R., Wagner, P., Frohlich, D., Weinberg, K., 2019. Dynamic fracture investigations of ultra-high performance concrete by spalling tests. Eng. Struct. 201, 109844.
Lak, M., Marji, M.F., Bafghi, A.Y., Abdollahipour, A., 2019. Analytical and numerical modeling of rock blasting operations using a two-dimensional elasto-dynamic Green's function. Int. J. Rock Mech. Min. Sci. 114, 208–217.
Li, J.C., Ma, G.W., 2009. Experimental study of stress wave propagation across a filled rock joint. Int. J. Rock Mech. Min. Sci. 46 (3), 471–478.
Li, J.C., Li, H.B., Zhao, J., 2015. An improved equivalent viscoelastic medium method for wave propagation across layered rock masses. Int. J. Rock Mech. Min. Sci. 73, 62–69.
Li, J.C., Li, N.M., Li, H.B., Zhao, J., 2017. An SHPB test study on wave propagation across rock masses with different contact area ratios of joint. Int. J. Impact Eng. 43 (105), 109–116.
Li, J.C., Rong, L.F., Li, H.B., Hong, S.N., 2019. An SHPB test study on stress wave energy attenuation in jointed rock masses. Rock Mech. Rock Eng. 52 (2), 403–420.
Li, J.C., Yuan, W., Li, H.B., Zou, C.J., 2022. Study on dynamic shear deformation behaviors and test methodology of sawtooth-shaped rock joints under impact load. Int. J. Rock Mech. Min. Sci. 158, 105210.
Liu, S., Xu, J.Y., 2013. Study on dynamic characteristics of marble under impact loading and high temperature. Int. J. Rock Mech. Min. Sci. 62, 51–58.
Liu, S., Xu, J.Y., 2015. Effect of strain rate on the dynamic compressive mechanical behaviors of rock material subjected to high temperatures. Mech. Mater. 82, 28–38.
Lukic, B., Saletti, D., Forquin, P., 2020. Validation of the photomechanical spalling test in the case of non-linear dynamic response: Application to a granite rock. Strain 56 (6), e12363.
Li, X.B., Tao, M., Wu, C.Q., Kun, D., Wu, Q.H., 2017. Spalling strength of rock under different static pre-confining pressures. Int. J. Impact Eng. 99, 69–74.
Li, X., Li, X.F., Zhang, Q.B., Zhao, J., 2018. A numerical study of spalling and related rockburst under dynamic disturbance using a particle-based numerical manifold method (PNMM). Tunn. Undergr. Space Technol. 81, 438–449.
Li, X.L., Wu, Y.B., He, L.H., Zhang, X.H., Wang, J.G., 2022. Research on dynamic properties of deep marble influenced by high temperature. Mathematics 10 (15), 2603.
Meyers, M.A., 1994. Dynamic Behavior of Materials. John Wiley & Sons, Inc.
Mitelman, A., Elmo, D., 2016. Analysis of tunnel support design to withstand spalling induced by blasting. Tunn. Undergr. Space Technol. 51, 354–361.
Niu, L.L., Zhu, W.C., Li, S.H., Guan, K., 2018. Determining the viscosity coefficient for viscoelastic wave propagation in rock bars. Rock Mech. Rock Eng. 51 (5), 1347–1359.
Niu, L.L., Zhu, W.C., Li, S., Liu, X.G., 2020. Spalling of a one-dimensional viscoelastic bar induced by stress wave propagation. Int. J. Mech. Min. Sci 131, 1004317.
Pathiranagei, S.V., Gratchev, I., 2022. Coupled thermo-mechanical constitutive damage model for sandstone. J. Rock Mech. Geotech. Eng. 14 (6), 1710–1721.
Rang, Z.D., Sun, W., 2012. Experimental and numerical investigation on the dynamic tensile behavior of ultra-high performance cement based composites. Constr. Constr. Build. Mater 31, 168–173.
Rossi, E., Kant, M.A., Madonna, C., Sarr, M.o., von Rohr, P.R., 2018. The effects of high heating rate and high temperature on the rock strength: feasibility study of a thermally assisted drilling method. Rock Mech. Rock Eng. 51 (9), 2957–2964.
Shao, S.S., Rangith, P.G., Wasantha, P.L.P., Chen, B.K., 2015. Experimental and numerical studies on the mechanical behaviour of Australian Strathbogie granite at high temperatures: An application to geothermal energy. Geothermics 54, 96–108.
Saadati, M., Forquin, P., Weddfelt, K., Larsson, P.L., 2016. On the tensile strength of granite at high strain rates considering the influence from preexisting cracks. Adv. Master. Sci. Eng 2016, 6279571.
Tao, M., Ma, A., Peng, K., Wang, Y.Q., Du, K., 2019. Fracture evaluation and dynamic stress concentration of granite specimens containing elliptic cavity under dynamic loading. Energies 12 (18), 3441.
Wang, Z.L., Yang, D., 2015. Study on dynamic behavior and tensile strength of concrete using 1D wave propagation characteristics. Mech. Adv. Mater. Struct. 22 (3), 184–191.
Wang, S.W., Li, J.C., Li, X., He, L., 2022a. Dynamic photoelastic experimental study on the influence of joint surface geometrical property on wave propagation and stress disturbance. Int. J. Rock Mech. Min 149, 104985.
Wang, Y.H., Wang, X.F., Liu, G.J., Tan, Y.Z., Zheng, Q.P., Zhao, Y.S., Zhang, Y.Y., 2021. Experiments on the one-dimensional spall strength of SFRC. Construct. Build. Mater. 280, 122110.
Wang, L.J., Fan, L.F., Du, X.L., 2022b. Non-attenuation behavior of stress wave propagation through a rock mass. Rock Mech. Rock Eng. 55 (7), 3807–3815.
Wu, H.J., Zhang, Q.M., Huang, F.L., Jin, Q.K., 2005. Experimental and numerical investigation on dynamic tensile strength of concrete. Int. J. Impact Eng. 32, 605–617.
Wu, H., Ren, G.M., Fang, Q., Liu, J.Z., 2018. Effects of steel fiber content and type on dynamic tensile mechanical properties of UHPCC. Construct. Build. Mater. 173, 251–261.
Wu, Y., Yin, T.B., Liu, X.L., Tan, X.S., Yang, Z., Li, Q., 2022. Determination of dynamic mode I fracture toughness of rock at ambient high temperature using notched semi-circular bend method. Trans. Nonferrous Metals Soc. China 32 (9), 3036–3050.
Xie, H.P., Zhu, J.B., Zhou, T., Zhang, K., Zhou, C.T., 2020. Conceptualization and preliminary study of engineering disturbed rock dynamics. Geomech. Geophys. Geo-Energy Geo-Resour 6 (2), 34.
Yang, S.Q., Ranjith, P.G., Jiang, H.W., Tian, W.L., Ju, Y., 2017. An experimental investigation on thermal damage and failure mechanical behavior of granite after exposure to different high temperature treatments. Geothermics 65, 180–197.
Yin, T.B., Wang, C., Wu, Y., Wu, B.Q., 2021. A waveform modification method for testing dynamic properties of rock under high temperature. J. Rock Mech. Geotech. Eng. 13 (4), 833–844.
Zhao, Q.B., Zhao, J., 2012. Determination of mechanical properties and full-field strain measurements of rock material under dynamic loads. Int. J. Rock Mech. Min. Sci. 60, 423–439.
Zhao, H.T., Tao, M., Li, X.B., Cao, W.Z., Wu, C.Q., 2019. Estimation of spalling strength of sandstone under different pre-confining pressure by experiment and numerical simulation. Int. J. Impact Eng. 133, 103359.
Zhang, J.Y., Ren, H.Q., Han, F., Sun, G.J., Wang, X., Zhao, Q., Zhang, L., 2020. Spall strength of steel-fiber-reinforced concrete under one-dimensional stress state. Mech. Mater. 141, 103273.
Zhang, J.Y., Shen, Y.J., Yang, G.S., Zhang, H., Wang, Y.Z., Hou, X., Sun, Q., Li, G.Y., 2021. Inconsistency of changes in uniaxial compressive strength and P-wave velocity of sandstone after temperature treatments. J. Rock Mech. Geotech. Eng. 13 (1), 143–153.
Zhu, J., Sun, C., Qian, Z., Chen, J.Y., 2011. The spalling strength of ultra-fiber reinforced cement mortar. Eng. Fail. Anal. 18 (7), 1808–1817.

Prof. Lifeng Fan is a professor at Beijing University of Technology. He is an editor of *Journal of Rock Mechanics and Geotechnical Engineering* (JRMGE) and other 4 journals. His research interest includes rock dynamics and seismic wave propagation in rock mass. He has led four National Natural Science Foundations of China, Beijing Science Fund for Distinguished Young Scientists and participated in some national projects. He has published more than 100 papers, 3 books and authorized more than 20 patents of invention.